Giant barocaloric effect in all-d-metal Heusler shape memory alloys.

Araceli Aznar,[1] Adrià Gràcia-Condal,[2] Antoni Planes,[2] Pol Lloveras,[1,*] Maria Barrio,[1]
Josep-Lluís Tamarit,[1] Wenxin Xiong,[3] Daoyong Cong,[3,†] Catalin Popescu,[4] and Lluís Mañosa[2,‡]

[1]*Departament de Física, EEBE, Campus Diagonal-Besòs and Barcelona Research Center in Multiscale Science and Engineering, Universitat Politècnica de Catalunya, Eduard Maristany, 10-14, 08019 Barcelona, Catalonia.*
[2]*Departament de Física de la Matèria Condensada, Facultat de Física, Martí i Franquès 1, Universitat de Barcelona, 08028 Barcelona, Catalonia.*
[3]*State Key Laboratory for Advanced Metals and Materials, University of Science and Technology Beijing, No. 30 Xueyuan Road, Haidian District, Beijing 100083, People's Republic of China.*
[4]*CELLS-ALBA Synchrotron, 08290 Cerdanyola del Vallès, Catalonia, Spain.*

(Dated: February 26, 2019)

We have studied the barocaloric properties associated with the martensitic transition of a shape memory Heulser alloy $Ni_{50}Mn_{31.5}Ti_{18.5}$ which is composed of all-d-metal elements. The composition of the sample has been tailored to avoid long range ferromagnetic order in both ausenite and martensite. The lack of ferromagnetism results in a weak magnetic contribution to the total entropy change thereby leading to a large transition entropy change. The combination of such a large entropy change and a relatively large volume change at the martensitic transition gives rise to giant barocaloric properties in this alloy. When compared to other shape memory Heusler alloys, our material exhibits values for adiabatic temperature and isothermal entropy changes significantly larger than values reported so far for this class of materials. Furthermore, our $Ni_{50}Mn_{31.5}Ti_{18.5}$ also compares favourably to the best state-of-the-art magnetic barocaloric materials.

PACS numbers: 64.70K,75.30 Sg

I. INTRODUCTION

Shape memory materials undergo a martensitic transition from a high temperature high symmetry cubic phase (austenite) to a low temperature lower symmetry close-packed phase (martensite). The occurrence of this structural transition confers these alloys a unique thermomechanical behaviour which is at the origin of a series of functional properties such as shape memory, pseudoelasticity and superelasticity[1]. More recently, giant magnetocaloric[2,3] and mechanocaloric effects[4,5] have also been reported to occur in shape memory alloys which make them excellent candidates for environmentally friendly solid state refrigeration technologies[6,7].

For non magnetic alloys, the structural change at the martensitic transition is mostly described by a shear of $\{110\}$ planes along the $[1\bar{1}0]$ direction of the cubic phase, with a negligible volume change[8]. Therefore the martensitic transition in these alloys is strongly sensitive to uniaxial stress (either compressive or tensile) but almost insensitive to hydrostatic pressure, and these alloys exhibit giant elastocaloric effects but negligible barocaloric effects[9]. However, in magnetic shape memory alloys the strong coupling between magnetism and structure results in noticeable volume changes at the phase transition which may give rise to giant barocaloric effects[5].

In their austenitic phase most magnetic shape memory alloys exhibit a Heusler structure with d-group elements (Ni and Mn) at the 8c (Ni) and 4a (Mn) positions (in Wyckoff notation), and p-group atoms (Ga, Sn, In,...) at the 4b positions[10]. Recently magnetic shape memory Heusler alloys have been developed with all-d-metal elements[11,12]. In these alloys Ti replaces p-group elements and it has been proved that the d-metal Ti provides a stabilization of the Heusler structure by d-d hybridization between Ti at 4b position and its nearest-neighbour element at the 8c or 4a position[12]. An interesting property of these all-d-group magnetic shape memory alloys is the large relative volume change at their martensitic transition which is significantly larger than for any other magnetic shape memory alloy. This peculiarity points to a marked sensitivity of the transition to the application of mechanical stresses, and particularly to an hydrostatic pressure, thereby making these materials excellent candidates to exhibit giant barocaloric effects.

The giant magnetocaloric and mechanocaloric effects exhibited by shape memory alloys originate from the first-order martensitic transition which involves a significantly large entropy change (ΔS_t). While in non magnetic alloys the entropy is mainly due to lattice vibration (phonon contribution), in magnetic shape memory alloys there is also a contribution from magnetic degrees of freedom which usually competes with the vibrational term[13], in such a way that the transition entropy change decreases as the austenite becomes more and more ferromagnetically ordered[14]. This competing scenario provides a dilemma[15] because on the one hand large entropy changes are desirable for caloric effects but on the other hand large magnetization and volume changes are also required for a good tunability of the transition temperature with external field and pressure. While magnetic order seems to be unavoidable to achieve giant magnetocaloric properties, it would be desirable to find shape memory alloys with large volume changes and weak mag-

netic order since they would exhibit enhanced barocaloric properties. In this work we report on a material meeting these requirements.

We have developed a Heusler alloy formed by all-d-elements (Ni, Ti and Mn). The composition has been tailored such that the alloy undergoes a martensitic transition slightly below room temperature. The interplay between magnetism and structure results in a relatively large volume change at the martensitic transition. However, the absence of ferromagnetic order results in a weak magnetic contribution to the entropy giving rise to a large transition entropy change. It is shown that this combination of large entropy and volume changes at the martensitic transition brings about outstanding barocaloric performances to this alloy.

II. EXPERIMENTAL DETAILS

Polycrystalline button ingots were prepared by arc-melting pure Ni, Mn and Ti elements in a high-purity Ar atmosphere. A small amount of B was also added to enhance the grain boundary cohesion and to improve the mechanical properties[16]. The ingots were sealed into evacuated quartz tubes and annealed at 1173 K for 48 h to ensure homogenization, followed by water quenching. The nominal composition of the sample was $(Ni_{50}Mn_{31.5}Ti_{18.5})_{99.8}B_{0.2}$. For the sake of simplicity in the following we will label our sample $Ni_{50}Mn_{31.5}Ti_{18.5}$.

A sample with dimensions 8.86 × 8.81 × 5.92 mm^3 was cut from the ingot for calorimetric measurements under hydrostatic pressure (barocaloric measurements). Smaller samples were also cut for conventional differential scanning calorimetry (DSC) and magnetic measurements. A number of these small samples were ground to produce powder for x-ray measurements. These powdered samples were further annealed under vacuum at 773 K for 5 h in order to minimise internal strains.

High-pressure powder diffraction experiments were performed at beamline BL04-MSPD at CELLS-ALBA synchrotron using a monochromatic beam of $\lambda = 0.4246$ Å[17]. The beamline is equipped with Kirkpatrick-Baez mirrors to focus the x-ray beam down to 20 × 20 μm^2 (FWHM). The sample was loaded into a membrane diamond anvil cell (DAC) of 400 μm culet size. The pressure chamber was a 200 μm hole drilled on a 45-μm preintented stainless steel gasket. NaCl powder was used as pressure marker[18]. A cryostat was used to control the temperature of the DAC. The sample-to-detector distance (200 mm) and the beam centre position were calibrated using FIT2D software[19] from LaB_6 diffraction data measured in the same conditions as the sample.

Conventional DSC measurements were performed with a Q2000 TA Instruments calorimeter, and magnetic measurements were performed using Superconducting Quantum Interference Device (SQUID) magnetometer. For the thermomagnetization measurements, the heating and cooling rates were 1 K min^{-1}. Calorimetry under hydrostatic pressure was carried out by means of a bespoke experimental device based on a Cu-Be pressure cell (operating up to 6 kbar) adapted as differential thermal analyser (DTA) by using Peltier modules as thermal sensors[20]. DW-Therm M0.200.02 (Huber Kältemaschinenbau GmbH) was used as pressure-transmitting liquid. The temperature was controlled by an external circulating thermal bath (Lauda Proline RP 1290, 183-473 K) and typical temperature rates of ∼ 2 K min^{-1} were chosen.

III. RESULTS AND DISCUSSION

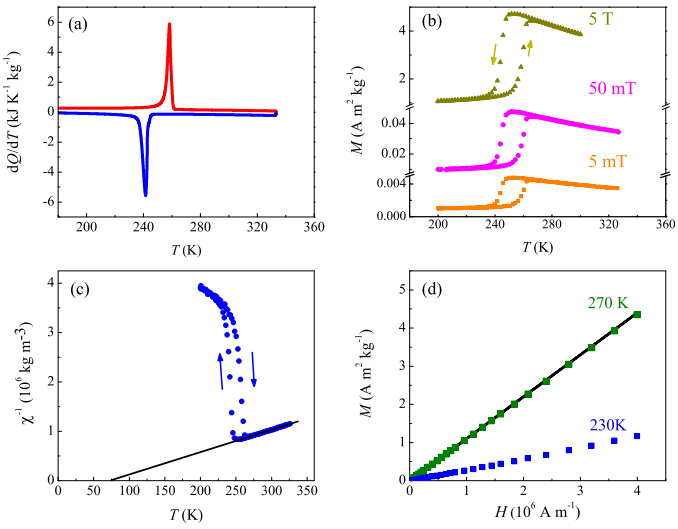

FIG. 1: (a) Differential scanning calorimetry curves on cooling (bottom curve) and heating (upper curve) runs. (b) Temperature dependence of the magnetization measured under different applied magnetic fields. (c) Inverse of the magnetic susceptibility as a function of temperature (line is a linear fit to the data in the austenitic phase). (d) Isothermal magnetization as a function of magnetic field in austenite (green) and martensite (blue). Black solid line corresponds to the predicted Curie-Weiss behaviour computed using T_c and μ determined from susceptibility data.

DSC curves taken at a temperature rate 5 Kmin^{-1} across the martensitic transition of $Ni_{50}Mn_{31.5}Ti_{18.5}$ are shown in Fig. 1a. Lower curve corresponds to the exothermal transition on cooling (forward martensitic transition) and upper curve, to the endothermal transition on heating (reverse martensitic transition). By taking the characteristic transition temperature (T_t) as the peak temperature of each DSC curve we obtain 243 K and 255 K for the forward and reverse transitions, respectively, with a 12 K thermal hysteresis. The latent heat of the transition is obtained by integration of DSC curves, with values of -20.8 ± 1.0 kJ kg^{-1} and 19.4 ± 1.0 kJ kg^{-1}, which correspond to transition entropy changes (ΔS_t) of -85 ± 6 J kg^{-1} K^{-1} and 76 ± 5 J kg^{-1} K^{-1} for

the forward and reverse transitions, respectively,.

Fig. 1b shows the temperature dependence of the magnetization upon cooling and heating at selected values of the magnetic field. The martensitic transition is clearly observed as a sharp decrease (increase) in magnetization on cooling (heating). For the studied range (up to 5 T) there is no noticeable shift in the martensitic transition with magnetic field, and transition temperatures are in good agreement with those determined from DSC. Fig. 1c displays the inverse of magnetic susceptibility χ^{-1} as a function of temperature computed from magnetization data at 5 mT. The linear increase of χ^{-1} with increasing temperature observed at high temperatures points to a paramagnetic behaviour of the austenite. A fit of a Curie-Weiss dependence to the data renders a magnetic moment per formula unit $\mu = 5.6\ \mu_B$ and a paramagnetic Curie temperature $T_c = 74$ K. It is worth noticing that T_c can be affected by a considerable error because it is obtained from the extrapolation of a linear fit to a set of data which are at temperatures far from T_c. In the austenitic phase the magnetization linearly increases with magnetic field, as illustrated in Fig. 1d, which shows measured isothermal magnetization at 270 K as a function of magnetic field. Actually, the reliability of μ and T_c derived from low field susceptibility data is confirmed by the excellent agreement found between experimental M vs H data (solid green symbols) and the predicted Curie-Weiss behaviour using $\mu = 5.6\ \mu_B$ and $T_c = 74$ K , which is plotted as a black line in Fig. 1d. Furthermore it has been reported that the austenitic phase of $Ni_{50}Mn_{50-x}Ti_x$ is antiferromagnetic for $x \geq 20$ [11]. For our sample $x = 18.5$ and the austenitic phase is paramagnetic. Magnetization in martensite is significantly lower than in austenite, and although the isothermal magnetization (at 230 K) also increases linearly with increasing magnetic field (with a slope lower than in austenite) the lack of paramagnetic behaviour in χ^{-1} and the weaker magnetic field dependence of the magnetization point to the existence of antiferromagnetic correlations in martensite, as reported for the martensitic phase in other magnetic shape memory alloys[21]

Diffraction patterns recorded at high temperature (299 K) and low temperature (200 K) and atmospheric pressure are shown in Fig. 2a. The austenite can be indexed as a cubic ($Fm\bar{3}m$) structure and the martensite is well described by an orthorhombic structure (Pmma). The lattice parameters were obtained by identifying the peak positions and using Win_Afmail software (included in Win_Cell package)[22]. We obtained a = 5.938(2) Å, for the cubic austenite, and a = 8.544(43) Å, b = 5.523 (35) Å, and c = 4.376(18) Å, for the orthorhombic martensite. Diffraction patterns were also recorded along one isobaric cooling ramp at atmospheric pressure (Fig. 2b) and at 9 kbar (Fig. 2c). At room temperature and atmospheric pressure the sample is in the austenitic state (with a small amount of retained martensite) and below ∼215 K diffraction peaks from the low temperature orthorhombic phase begin to develop. At the lowest temperature the

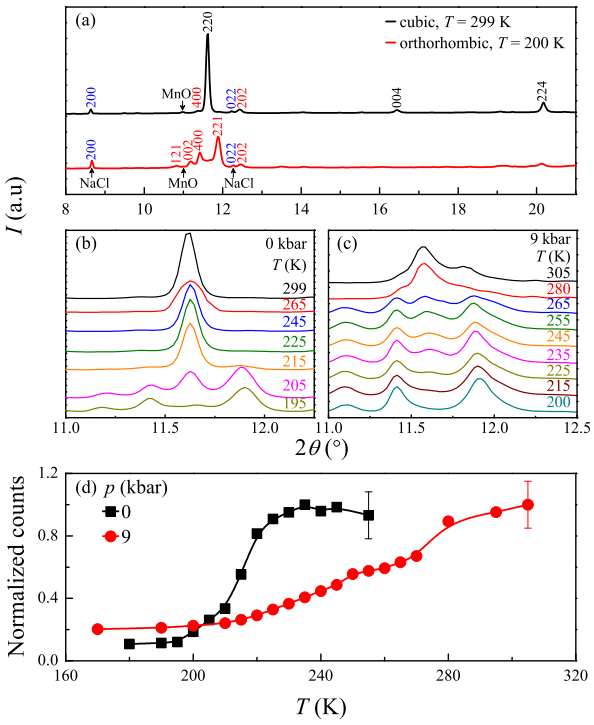

FIG. 2: (a) Diffraction patterns in the austenite (299 K, black line) and in the martensite (200 K, red line), with indexation of the peaks corresponding to the cubic (black labels) and orthorhombic (red labels) phases for austenite and martensite, respectively. Peaks from NaCl and MnO are also indicated. (b) and (c) isobaric evolution of selected diffraction patterns obtained on cooling at atmospheric pressure and under 9 kbar, respectively. (d) Normalized number of counts of the 220 peak of the cubic phase as a function of temperature for atmospheric pressure (black squares) and for 9 kbar (red circles). Lines are guides to the eye. For clarity only a typical error bar is shown for each run.

sample is in the orthorhombic phase although a small peak from the cubic austenite is still present. For an applied pressure of 9 kbar the sample is predominantly in the austenitic phase at room temperature. There is some presence of martensitic phase in a larger amount than at atmospheric pressure. Upon cooling, diffracion peaks from the martensitic structure start to grow at $T \sim$ 265 K, and at the lowest measured temperature (200 K) the sample is in the martensitic phase.

A simple and straightforward analysis of the evolution of the martensitic transition can be achieved by monitoring the intensity of the 220 cubic peak. In Fig. 2d we plot the number of counts normalized by the value at ambient temperature, for atmospheric pressure and 9 kbar. The shift of the martensitic transition towards higher temperatures with applied pressure is clear from the data. The transition at atmospheric pressure is sharp, but under applied pressure it spreads over a broader temperature range. The spreading of the transition is not a particular effect of Ni-Mn-Ti but rather it is related to non

hydrostatic stress due to the choice of NaCl as a pressure transmitting medium.

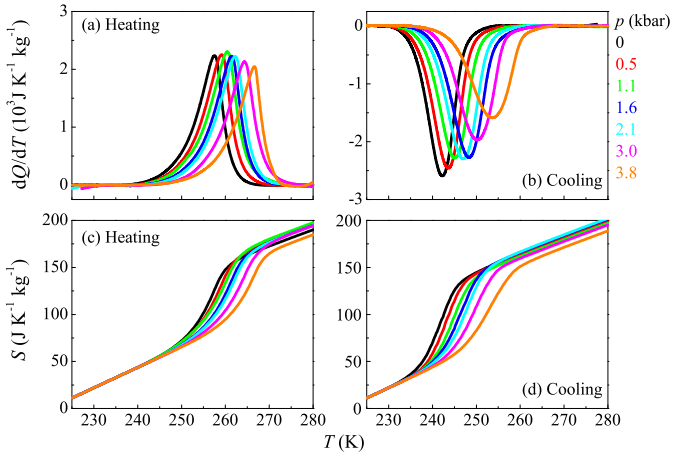

FIG. 3: Calorimetric curves at selected values of applied hydrostatic pressure recorded during heating (a) and cooling (b) runs. Entropy (with respect to the entropy at $T_0 = 220$ K) as a function of temperature for selected values of applied hydrostatic pressure for heating (c) and cooling (d) runs.

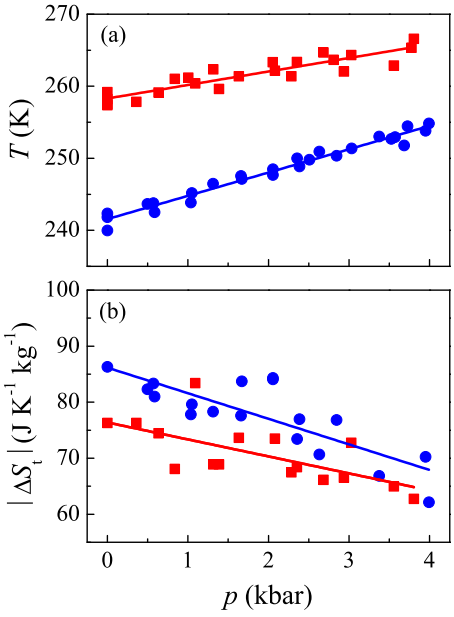

FIG. 4: (a) Transition temperature and (b) transition entropy change as a function of pressure. Blue symbols stand for the forward transition and red symbols stand for the reverse transition. Lines are linear fits to the data.

Illustrative examples of the baseline-corrected calorimetric curves obtained under constant hydrostatic pressure are shown in Fig. 3a (heating runs) and Fig. 3b (cooling runs). Application of pressure shifts the martensitic transition to higher temperatures, as shown in Fig. 4a where we plotted the peak temperature of calorimetric curves as a function of hydrostatic pressure, for both forward and reverse martensitic transitions. The increase in transition temperatures is linear, with slopes $dT/dp = 3.2 \pm 0.1$ K kbar^{-1} and $dT/dp = 1.9 \pm 0.1$ K kbar^{-1} for forward and reverse transitions, respectively.

The transition entropy change is computed as

$$\Delta S_t = \int_{T_1}^{T_2} \frac{1}{T}\frac{dQ}{dT}dT \qquad (1)$$

where $\frac{dQ}{dT} = \frac{\dot{Q}}{|\dot{T}|}$, and T_1 and T_2 are freely chosen temperatures below and above the martensitic transition respectively. The values obtained are plotted as a function of pressure in Fig. 4b, which shows a decrease in $|\Delta S_t|$ with increasing hydrostatic pressure, this decrease being more pronounced for the forward transition. A linear fit to the data gives $d|\Delta S_t|/dp$ = -4.4 ± 0.8 J K^{-1} kg^{-1} kbar^{-1} for the forward transition and $d|\Delta S_t|/dp$ = -2.6 ± 0.9 J K^{-1} kg^{-1} kbar^{-1} for the reverse transition.

Following the procedure described in ref. [9] we have computed the barocaloric effect using our calorimetric data under hydrostatic pressure (Figs. 3a and 3b) and specific heat data at atmospheric pressure[23] (which is assumed to be pressure independent).

We first obtained the entropy vs temperature curves at selected values of applied hydrostatic pressure from

$$S(T,p) = \begin{cases} \int_{T_0}^{T} \frac{C_p^M}{T}dT & T \le T_1 \\ S(T_1,p) + \int_{T_1}^{T} \frac{1}{T}\left(C_p + \frac{dQ}{dT}\right)dT & T_1 < T \le T_2 \\ S(T_2,p) + \int_{T_2}^{T} \frac{C_p^A}{T}dT & T_2 < T \end{cases} \qquad (2)$$

where C_p^M and C_p^A are, respectively the specific heat of martensite and austenite, and $C_p = xC_p^M + (1-x)C_p^A$ where x is the fraction of martensite. The other quantities have the same meaning as explained before. $S(T,p)$ represents the entropy referred to the value at a selected temperature of $T_0 = 220$ K. The obtained entropy curves are shown in Figs. 3c and 3d for reverse and forward transitions respectively. The scatter in transition entropy values (Fig. 4b) gives rise to a relative error in $S(T,p)$ at high temperatures in the range 8-10%, and therefore the small differences in the entropy of the austenitic phase for different applied pressures (Figs. 3c and d) are not relevant.

From these entropy curves it is straightforward to compute the isothermal entropy change induced by the application of a pressure p as:

$$\Delta S(T, 0 \to p) = S(T,p) - S(T,0), \qquad (3)$$

and the adiabatic temperature change as:

$$\Delta T(S, 0 \rightarrow p) = T(S, p) - T(S, 0) \qquad (4)$$

For a release of pressure ($p \rightarrow 0$), equivalent expressions hold.

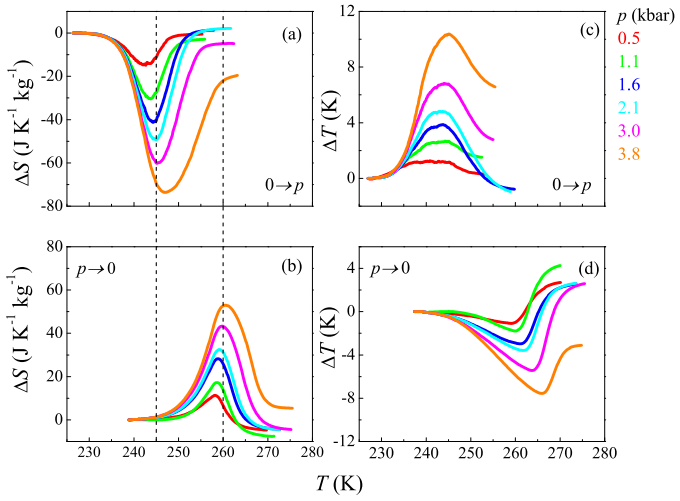

FIG. 5: Isothermal entropy changes corresponding to the removal (a) and application (b) of selected values of hydrostatic pressure. Vertical dashed lines indicate the reversibility region. Adiabatic temperature changes corresponding to the removal (c) and application (d) of selected values of hydrostatic pressure.

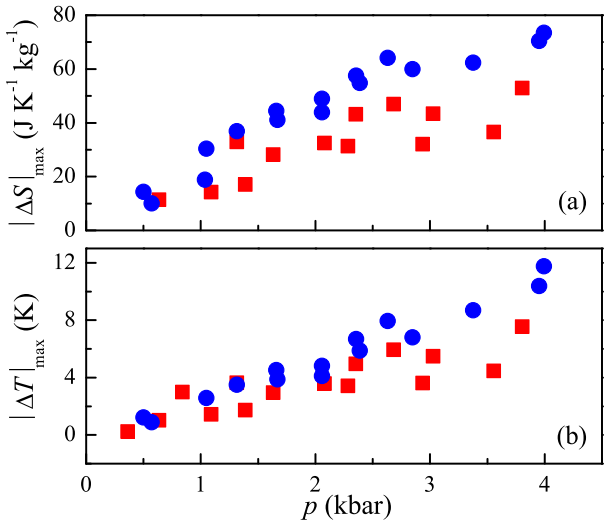

FIG. 6: (a) Maximum isothermal entropy change, and (b) maximum adiabatic temperature change. Red symbols correspond to the reverse transition upon application of pressure and blue symbols correspond to the forward transition upon removal of pressure.

Since pressure stabilizes the martensitic phase (as cooling does) the entropy and temperature changes induced by applying a pressure p are computed from calorimetric curves on cooling. Similarly, a release of a pressure p promotes the transition from martensite to austenite and therefore entropy and temperature changes in that case are computed from heating curves. Results are shown in Fig. 5. As reported for other magnetic shape memory alloys, the barocaloric effect in $Ni_{50}Mn_{31.5}Ti_{18.5}$ is conventional, i.e. isothermal application (removal) of pressure reduces (increases) entropy and adiabatic application (removal) of pressure increases (decreases) temperature. It is found that the maximum values for the isothermal entropy change ($|\Delta S|_{max}$) and adiabatic temperature change ($|\Delta T|_{max}$) increase as pressure increases, as illustrated in Fig. 6. For all pressures, values for $|\Delta S|_{max}$ and $|\Delta T|_{max}$ are larger for the forward transition than for the reverse one. The difference is ascribed to a larger transition entropy change and a stronger sensitivity of the transition temperature to pressure.

Application of barocaloric materials to refrigeration technologies requires a good reversibility of their barocaloric effect under cyclic application and removal of pressure. Such a reversibility near a first-order transition depends on the competition between the width of thermal hysteresis and the sensitivity of transition temperatures upon pressure. For a conventional barocaloric effect reversible barocaloric effects have been shown to occur within a temperature interval bounded by the start of the reverse transition on heating at atmospheric pressure and the start of the forward transition on cooling under an applied pressure[25,29]. Within this temperature region application and removal of pressure carries the state of the material through minor hysteresis loops, and the reversibility in the barocaloric effect is directly related to the reversibility in the fraction of material that undergoes the forward and reverse transtitions in each cycle. For our $Ni_{50}Mn_{31.5}Ti_{18.5}$ the reversibility region (indicated by dashed vertical lines in Figs. 5a and 5b) spans from 245 K to 260 K, and the maximum estimated reversible isothermal entropy change within this region amounts $|\Delta S_{rev}| \simeq 35$ J kg^{-1} K^{-1}.

The barocaloric effect has recently been studied in different shape memory Heusler alloys. In Table 1 we compare present results for $Ni_{50}Mn_{31.5}Ti_{18.5}$ to those reported for other shape memory Heusler alloys[5,24–28] for which we have listed the largest reported entropy and temperature change values (corresponding either to the first application or first removal of pressure). It is clear that our $Ni_{50}Mn_{31.5}Ti_{18.5}$ exhibits the largest $|\Delta S|_{max}$ and $|\Delta T|_{max}$ values among all shape memory Heusler alloys. Furthermore, $|\Delta S_{rev}|$ is also larger than reversible values reported for other shape memory Heusler alloys[25].

In Fig. 7 we compare our values for isothermal entropy change and adiabatic temperature change to those reported for state-of-the-art magnetic barocaloric

TABLE I: Sample composition, transition entropy change $|\Delta S_t|$, applied pressure Δp, isothermal entropy change $|\Delta S|_{max}$, adiabatic temperature change $|\Delta T|_{max}$, and refrigerant capacity RC.

Sample	$\lvert\Delta S_t\rvert$ ($Jkg^{-1}K^{-1}$)	$\frac{dT}{dp}$ (K $kbar^{-1}$)	Δp (kbar)	$\lvert\Delta S\rvert_{max}$ ($Jkg^{-1}K^{-1}$)	$\lvert\Delta T\rvert_{max}$ (K)	RC (Jkg^{-1})	Reference
$Ni_{49.26}Mn_{36.08}In_{14.66}$	27	1.8	2.6	24.4	–	–	5
$Ni_{51.2}Mn_{32.5}In_{16.3}$	40.8	1.65	2.5	32	4	200	25
$Ni_{42.47}Co_{8.87}Mn_{31.67}Ga_{14.98}In_{2.01}$	22.8	3.2	2.5	16	–	200	24
$Ni_{58.3}Mn_{17.1}Ga_{24.6}$	16	0.4	10	13.5	2.8	56	26
$Ni_{44.6}Co_{5.5}Mn_{35.5}In_{14.4}$	16	4.4	6	15.6	6	399	27
$Ni_{42.3}Co_{7.9}Mn_{38.8}Sn_{11.0}$	28	4.7	6	23	10	786	28
$(Ni_{50}Mn_{31.5}Ti_{18.5})_{99.8}B_{0.2}$	85	3.3	4	74	12	1100	This work

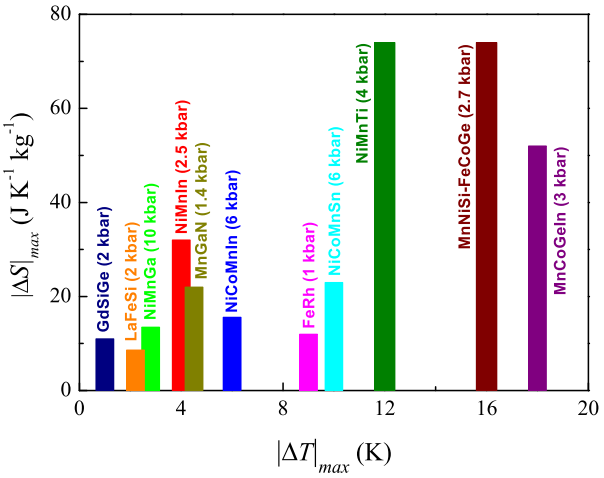

FIG. 7: Isothermal entropy and adiabatic temperature changes for state-of-the-art magnetic barocaloric materials. For the sake of clarity each material is designated by an indicative label and not by its actual composition. All data are obtained from calorimetric measurements (quasi-direct method) except $|\Delta T|_{max}$ for GdSiGe and LaFaSi which correspond to thermometric measurements. The minimum pressure required to obtain $|\Delta S|_{max}$ is indicated for each compound. Data correspond to the first application (or first removal) of pressure, and are extracted from refs.[25–34]

materials[25–34]. Because reversible values (upon repeatedly applying and removing pressure) are not reported for many of the materials, our comparison will be based on entropy and temperature values for the first application and first removal of pressure. It is apparent that $Ni_{50}Mn_{31.5}Ti_{18.5}$ exhibits the largest values, only comparable to those for hexagonal Ni_2In-type Mn-Co-Ge-In (and related) compounds[33,34]. However, compared to Ni_2In-type compounds our alloy exhibits much better mechanical properties. While Ni_2In-type compounds rapidly degrade when cycled through the transition (owing to the large volume change at the magnetostructural transition) and bulk samples pulverize, our $Ni_{50}Mn_{31.5}Ti_{18.5}$ has an excellent stability in their thermodynamic and structural properties[23].

In addition to magnetic alloys, giant barocaloric effects have also been reported in a broad variety of materials including ferroelectric[35–37] and ferrielectric[38] materials, fluorides[39,40], hybrid perovskites[41] and superionic conductors[42]. Among all these materials only $(NH_4)_2NbOF_5$[40] exhibits an isothermal entropy change ($\Delta S = 100$ J kg^{-1} K^{-1}) larger than the value found for our $Ni_{50}Mn_{31.5}Ti_{18.5}$ shape memory Heusler alloy. However, the density of our material ($\rho = 7040$ kg m^{-3}) is almost 5 times larger than that of $(NH_4)_2NbOF_5$ ($\rho = 1450$ kg m^{-3})[9] which implies a much larger isothermal entropy change in our compound when normalized to volume. Furthermore metallic materials have a larger thermal conductivity which is desirable for practical and efficient solid-state refrigeration.

IV. SUMMARY AND CONCLUSIONS

We have studied the barocaloric properties of $Ni_{50}Mn_{31.5}Ti_{18.5}$, a shape memory Heusler alloy composed by all-d-metal elements. The composition has been tailored so that the sample undergoes a martensitic transition but it does not ferromagnetically order in any of the two structural phases. The entropy change at the martensitic transition is very large due to the weak magnetic contribution resulting from the absence of ferromangetic order. On the other hand the relatively large volume change at the martensitic transition gives rise to a marked pressure dependence of the transition temperatures. It has been shown that due to the combination of this pressure dependence and a large transition entropy change the alloy exhibits outstanding barocaloric performances. The values found for pressure induced isothermal entropy and adiabatic temperature changes, outperform those reported for other shape memory Heusler alloy, and are among the largest values reported for best state-of-the-art barocaloric materials.

Our $Ni_{50}Mn_{31.5}Ti_{18.5}$ alloy is composed of accessible materials. It exhibits an excellent behaviour under cycling which together with the outstanding barocaloric performances reported here places this alloy at the forefront of caloric materials to be used in clean solid-state refrigeration technologies.

Acknowledgements

We acknowledge financial support from CICyT (Spain) Projects N. MAT2016-75823-R and FIS2017-82625-P, and from AGAUR (Catalonia), Project 2017SGR-0042. D.Y.C. acknowledges support from the National Natural Science Foundation of China (Projects. Nr. 51822102 and 51731005) A.G. acknowledges financial support from Universitat de Barcelona under the APIF scholarship. Experimental support from E. Xuriguera is acknowledged.

* pol.lloveras@upc.edu
† dycong@ustb.edu.cn
‡ lluis.manosa@fmc.ub.edu

[1] K. Otsuka, C.M. Wayman *Shape Memory Materials*, Cambridge University Press, 1998.
[2] F.X. Hu, B.G. Shen, J.R. Sun, Appl. Phys. Lett. **76**, 3460 (2000).
[3] T. Krenke, E. Duman, M. Acet, E.F. Wassermann, X. Moya, L. Mañosa, A. Planes, Nat. Mater. **4**, 450 (2005).
[4] E. Bonnot, R. Romero, L. Mañosa, E. Vives, A. Planes, Phys. Rev. Lett. **100**, 125901 (2008).
[5] L. Mañosa, D. González-Alonso, A. Planes, E. Bonnot, M. Barrio, J.L. Tamarit, S. Aksoy, M. Acet, Nat. Mater. **9**, 478 (2010).
[6] L. Mañosa, A. Planes, M. Acet, J. Mater. Chem. A **1**, 4925 (2013).
[7] X. Moya, S. Kar-Narayan, N.D. Mathur, Nat. Mater. **13**, 439 (2014) .
[8] A. Planes, L. Mañosa, Solid State Phys. **55**, 159 (2001).
[9] L. Mañosa, A. Planes, Adv. Mater. **29**, 1603607 (2017).
[10] A. Planes, L. Mañosa, M. Acet, J. Phys.: Condens. Matter **21**, 233201 (2009).
[11] Z.Y. Wei, E.K. Liu, J.H. Chen, Y. Li, G.D. Liu, H.Z. Luo, X.K. Xi, H.W. Zhang, W.H. Wang, G.H. Wu, Appl. Phys. Lett. **107**, 022406 (2015).
[12] Z.Y. Wei, E.K. Liu, Y. Li, X.L. Han, Z.W. Du, H.Z. Luo, G.D. Liu, X.K. Xi, H.W. Zhang, W.H. Wang, G.H. Wu, Appl. Phys. Lett. **109**, 01904 (2016) .
[13] T. Kihara, X. Xu, W. Ito, R. Kainuma, M. Tokunaga, Phys. Rev. B **90**, 214409 (2014).
[14] V. Recarte, J.I. Pérez-Landazabal, V. Sánchez-Alarcos, V. Zablotskii, E. Cesari, S. Kustov, Acta Mater. **60**, 3168 (2012).
[15] T. Gottschall, K.P. Skokov, D. Benke, M.E. Gruner, O. Gutfleisch, Phys. Rev. B **93**, 184431 (2016).
[16] Z. Yang, D.Y. Cong, X.M Sun, Z.H. Nie, Y.D. Wang, Acta Mater. **127**, 33 (2017).
[17] F. Fauth, I. Peral, C. Popescu, M. Knapp, Powder Diffr. **28**, S360 (2013).
[18] P.I. Dorogokupets, A. Dewaele, High Pressure Res. **27**, 431 (2007).
[19] A.P. Hammersley, S.O. Svensson, A.N. Fitch, High Press. Res. **14**, 235 (1996).
[20] A detailed description of callibration protocols for DTA under pressure can be found in E. Stern-Taulats, PhD Thesis, Universitat de Barcelona 2017.
[21] S. Aksoy, M. Acet, P.P. Deen, L. Mañosa, A. Planes, Phys. Rev. B **79**, 212401 (2009).
[22] http://fazil.rejabalee.free.fr/delphi_an.htm.
[23] W. Xiong, unpublished.
[24] L. Mañosa, E. Stern-Taulats, A. Planes, P. Lloveras, M. Barrio, J.L. Tamarit, B. Emre, S. Yüce, S. Fabbrici, F. Albertini, Phys. Stat. Sol. B **251**, 2114 (2014).
[25] E. Stern-Taulats, A. Planes, P. Lloveras, M. Barrio, J.L. Tamarit, S. Pramanick, S. Majumdar, S. Yüce, B. Emre, C. Frontera, L. Mañosa, Acta Mater., **96**, 324 (2015).
[26] X.J. He, K. Xu, S.X. Wei, Y.L. Zhang, Z. Li, C. Jing, J. Mater. Sci. **52**, 2915 (2017).
[27] X.J. He, S.X. Wei, Y. Kang, Y. Zhang, Y. Cao, K. Xu, Z. Li, C. Jing, Scr. Mater. **145**, 58 (2018).
[28] X.J. He, Y.R. Kang, S.X. Wei, Y.L. Zhang, Y.M. Cao, K. Xu, Z. Li, C. Jing, Z.B. Li, J. Alloys and Compds. **741**, 821 (2018).
[29] E. Stern-Taulats, A. Planes, P. Lloveras, M. Barrio, J.L. Tamarit, S. Pramanick, S. Majumdar, C. Frontera, L. Mañosa, Phys. Rev. B **89**, 214105 (2014).
[30] L. Mañosa, D. González-Alonso, A. Planes, M. Barrio, J.L. Tamarit, I.S. Titov, M. Acet, A. Bhattacharyya, S. Majumdar, Nat. Comm. **2**, 595 (2011).
[31] D. Matsunami, A. Fujita, K. Takenaka, M. Kano, Nat. Mater. **14**, 73 (2015).
[32] S. Yüce, M. Barrio, B. Emre, E. Stern-Taulats, A. Planes, J.L. Tamarit, Y. Mudryk, K.A. Gschneidner, V.K. Pecharsky, L. Mañosa, Appl. Phys. Lett. **101**, 071906 (2012).
[33] R.R. Wu, L.F. Bao, F.X. Hu, H. H.Wu, Q.Z. Huand, J. Wang, X.L. Dong, G.N. Li, J. R. Sun, F.R. Shen, T.Y. Zhao, X.Q. Zheng, L.C. Wang, Y. Liu, W.L. Zuo, Y.Y. Zhao, M. Zhang, X.C. Wang. C.Q. Jin, G.H. Rao, X.F. Han, B.G. Shen, Sci. Rep. **5**, 18027 (2015).
[34] T. Samanta, P. Lloveras, A.U. Saleheen, D.L. Lepkowski, E. Kramer, I. Dubenko, P.W. Adams, D.P. Young, M. Barrio, J. Ll. Tamarit, N. Ali, S. Stadler, Appl. Phys. Lett. **112**, 021907 (2018).
[35] E. Stern-Taulats, P. Lloveras, M. Barrio, E. Defay, M. Egilmez, A. Planes, J.L. Tamarit, L. Mañosa, N.D. Mathur, X. Moya, APL Mater. **4**, 091102 (2016).
[36] E.A. Mikhaleva, I.N. Flerov, M.V. Gorev, M.S. Molokeev, A.V. Cherepakhin, A.V. Kartashev, N.V. Mikhashenov, K.A. Sablina, Phys. Sol. State **54**, 1832 (2012).
[37] Y. Liu, J. Wei, P.E. Janolin, I.C. Infante, X.J. Lou, B. Dkhil, Appl. Phys. Lett. **104**, 162904 (2014).
[38] P. Lloveras, E. Stern-Taulats, M. Barrio, J.L. Tamarit, S. Crossley, W. Li, V. Pomjakushin, A. Planes, L. Mañosa, N.D. Mathur, X. Moya, Nat. Comm. **6**, 8801 (2015).
[39] I.N. Flerov, A.V. Kartashev, M.V. Gorev, E.V. Bogdanov, S.V. Mel'nikolva, M.S. Molokeev, E.I. Pogoreltsev, N.M. Laptash, J. Fluorine Chem. **183**, 1 (2016).
[40] M.V. Gorev, E.V. Bogdanov, I.N. Flerov, Scr. Mater. **139**, 53-57 (2017).
[41] J.M. Bermúdez, M. Sánchez-Andújar, S. Castro-Garcia, J. López-Beceiro, R. Artiaga, M.A. Senaris-Rodríguez, Nat. Comm. **8**, 15715 (2017).
[42] A. Aznar, P. Lloveras, M. Romanini, M. Barrio, J.L. Tamarit, C. Cazorla, D. Errandonea, N.D. Mathur, A. Planes, X. Moya, L. Mañosa, Nat. Comm. **8**, 1851 (2017).